2015 – 2016
Laboratory : University of Utrecht – Institut de Physique du Globe de Paris
Department : Laboratoire de Sismologie, IPGP
Advisors : N. Fuji, H. Paulssen

Exploration of Galerkin methods for seismic wavefield modelling

Thijs Franken

Abstract

In this thesis, we explored the impact of trial functions of Galerkin finite element methods on seismic waveform modelling. If we use linear spline functions, the modelling will be the same as second-order finite difference. Here we propose the sinc functions instead in order to reconcile with the nature of wavefield. We derive formally the errors of operators and show the potential superiority of sinc function to spline functions. We tested numerical solutions for 1D SH cases. The future work is the optimisation of these operators (Geller & Takeuchi 1995) but since there have been no systematical recipe of optimisation, we reformulate the optimisation for future automatisation.

Key words : Synthetic seismogram, Galerkin methods, trial functions

Contents

1 Introduction

Seismology has been the prime tool for the investigation of the Earth's interior within the branches of geophysical imaging. Seismic waves can contain broadband frequencies of energy after intercting with the structure of the Earth's interior and experiences the least waveform distortion and amplitude attenuation compared to other observable geophysical phenomena [Aki and Richards, 2002]. These features enable seismic imaging to achieve superior resolution and accuracy compared to other geophysical methods such as heat flow, static displacement, strain, gravity and electromagnetic waves [Aki and Richards, 2002]. Combined with a large range in coverage from a local to a global scale it is a versatile methodology for both small scale shallow targets and great depth, which makes seismology a valuable method for both research and industrial purposes. Optimisation of seismic methodologies is therefore essential for improving the comprehension of the inter structure by improving model accuracy and aiding in cost reduction in these sectors.

One of the most powerful methods to extract information of the Earth's interior from seismic waves is seismic tomography. It uses a forward modelling approach to seismic imaging in combination with a non-linear inverse problem. During forward modelling, an initial model for the Earth's structure and properties is assumed, and according to ray theory, a prediction is made for the outcome of the observations in the form of synthetic travel-time data. The inverse problem, on the other hand, attempts to reconstruct the distribution of physical parameters that control seismic wave propagation from observed data into an Earth model [Thurber and Ritsema, 2007]. Inverting the waveform difference between the forward modelled synthetics and observed data allows computation of model perturbations through partial derivatives. The initial model used for forward modelling is enhanced through solving the inverse approach and is resubmitted in the forward scheme to generate an improved set of synthetics. The two approaches work in conjunction as an iterative process called Full Waveform Inversion (FWI) to refine the model parameters and the synthetics in a stepwise manner to minimise the misfit between the synthetic seismograms and the observed data [Tromp et al., 2005][Plessix, 2006]. Since computation of the synthetics and the partial derivatives are achieved through a forward modelling scheme, effective realisation of this method depends highly on the accuracy and efficiency of the numerical operators used for forward modelling.

Current forward modelling schemes for seismic wavefield simulation that are prevalent in exploration and global seismology are methods such as the Spectral Element Method (SEM: [Komatitsch and Vilotte, 1998]) and the Discontinuous Galerkin method (DG: [Käser and Dumbser, 2006]). By defining an unstructured grid mesh in a sophisticated manner, such methods can accurately cope with complex topography, a feat that a finite difference approach struggles with if not optimised. However, unstructured grid methods such as SEM and DG are still too costly, and meshing would be a burden for the realisation of FWI. Firstly, detailed information of the Earth structure is required for sophisticated mesh designing. Information which, besides surface topography and bathymetry, we do not have in such detail. Secondly, these methods rely on a computationally heavy meshing process that would have to be repeated for each iteration of the FWI, making the expenses for this method excessive. Instead, the numerical approach for forward modelling synthetic seismograms should rely on a simple and regular meshing process in order to viably attempt FWI; numerical methods such as the Finite Difference Method (FDM).

However, the conventional numerical schemes for a FDM approach come with numerical errors because of numerical dispersion. Geller & Takeuchi [Geller and Takeuchi, 1995][Geller and Takeuchi, 1998] have developed a method to optimise the operators of the equation of motion for a one-dimensional second order Finite-Difference (FD) scheme to remove the truncation errors. In this paper they use the Direct Solution Method, a form of the Finite Element Method (FEM), to display the elastic equation of motion in its Galerkin weak form [Strang and Fix,

1973], in order to deal with the spatial and temporal operators in the same framework. The operators are modified through a predictor-corrector scheme, which works in conjuction with the three-point FD scheme without altering the main engine.

In this master thesis we revisit the work of Geller & Takeuchi (1995; 1998) in order to explore the possibility of optimising operators for wave propagation when using higher order difference schemes. We study the Galerkin weak form of the elastic wave equation and review the methodologies of FD and FEM with regard to the trial functions used for three-point and five-point difference schemes. We introduce an alternate form of the trial function for grid interpolation that coincides better with the particle motion seen in wave propagation, assisted by numerical examples of their effect on the waveform operators for a three-point and five-point difference scheme in a 1D and 2D medium.

2 Theory

2.1 3D equation of motion for isotropic media

In this section we start with the strong form of the elastic equation of motion describing the propagation of a wavefield through a medium:

$$\rho \frac{\partial^2}{\partial t^2} u_i - \frac{\partial}{\partial x_j}\left(C_{ijkl} \frac{\partial u_k}{\partial x_l} \right) = f_i \tag{1}$$

where ρ is the density, C_{ijkl} the elastic moduli and are time-dependent when the medium is anelastic.

If the medium is isotropic, C_{ijkl} can be written as:

$$C_{ijkl} = \lambda \delta_{ij} \delta_{kl} + \mu \delta_{ik} \delta_{jl} + \mu \delta_{il} \delta_{jk} \tag{2}$$

with λ the Lamé parameter, μ the shear modulus and the i-th component of the displacement and excitation force are denoted by u_i and f_i. This expression can be rearranged to separate the homogeneous and heterogenous components of the elastic parameters:

$$\rho \frac{\partial^2}{\partial t^2} u_i - \left(\frac{\partial}{\partial x_j} C_{ijkl} \right) \frac{\partial u_k}{\partial x_l} - C_{ijkl} \frac{\partial^2 u_k}{\partial x_j \partial x_l} = f_i \tag{3}$$

with the heterogeneous component:

$$- \left(\frac{\partial}{\partial x_j} C_{ijkl} \right) \frac{\partial u_k}{\partial x_l} = \left(\frac{\partial}{\partial x_i} \lambda \right) \frac{\partial u_k}{\partial x_k} - \left(\frac{\partial}{\partial x_k} \mu \right) \frac{\partial u_k}{\partial x_i} - \left(\frac{\partial}{\partial x_j} \mu \right) \frac{\partial u_i}{\partial x_j} \tag{4}$$

and the homogeneous component:

$$- C_{ijkl} \frac{\partial^2 u_k}{\partial x_j \partial x_l} = \lambda \frac{\partial^2 u_k}{\partial x_i \partial x_k} - \mu \frac{\partial^2 u_k}{\partial x_k \partial x_i} - \mu \frac{\partial^2 u_i}{\partial^2 x_j}. \tag{5}$$

Decomposing the equation of motion for an isotropic medium achieves separation of wavefields into P-SV and SH wavefields. The last term in eq. 4 and of eq. 5 describe the elastic parameters for the SH case, while the P-SV case is defined by the remaining terms in the right hand side of the equations. The equation of motion for an SH wavefield can be written as:

$$\rho \frac{\partial^2}{\partial t^2} u_i - \frac{\partial}{\partial x_j} \mu \frac{\partial u_i}{\partial x_j} - \mu \frac{\partial^2 u_i}{\partial^2 x_j} = f_i \tag{6}$$

2.2 1D equation of motion for the SH case

We apply the Fourier transform from t to ω as:

$$A(\omega) = \int_{-\infty}^{\infty} dt A(t) \exp(-i\omega t) \tag{7}$$

from x to k_x as:

$$A(k_x) = \int_{-\infty}^{\infty} dt A(x) \exp(-ik_x x) \tag{8}$$

and from y to k_y as:

$$A(k_y) = \int_{-\infty}^{\infty} dt A(y) \exp(-ik_y y) \tag{9}$$

in order to focus on the wave propagation along z direction. For a 1D model along z, the Fourier transform of eq. 6 from the time- to frequency-domain, x to the k_x domain and y to k_y domain, yields:

$$(\rho\omega^2 - (k_x + k_y)^2\mu)u + \frac{\partial}{\partial z}\left(\mu\frac{\partial u}{\partial z}\right) = -f \tag{10}$$

Equation eq. 10 is the strong form of the equation of motion for a laterally homogenous SH problem in the frequency domain, where ω is the angular frequency acquired from the Fourier transformation of the second time-derivative in eq. 6 , and k_x and k_y the wavenumbers acquired through Fourier transforming the spatial derivative. Since there is no change in μ along the x-axis for the 1D model, the spatial derivative over x equals to zero and is omitted.

2.3 Discretisation

Numerical modelling of the seismic wavefield is performed through discretising the continuous equation of motion, which is an approximation to the solution of the continuous function. By representing the displacement u as a summation of trial functions a weak form of the equation of motion can be constructed from eq. 10.

$$u = \sum_{m}^{N} c_m \psi_m \quad (m = 0, ..., N) \tag{11}$$

where the displacement in one dimension u is represented as a combination of trial functions, with c_n as the eigenvector of the n-th node that exists in a finite space from 0 to N. Substituting eq. 11 into eq. 10 for this finite medium we obtain:

$$\int_{z_0}^{z_N} dz(\rho\omega^2 - k_x^2\mu - k_y^2\mu)\sum_m c_m\psi_m(z) + \frac{\partial}{\partial z}\left(\mu\frac{\partial}{\partial z}\sum_m c_m\psi_m(z)\right) = -\int_{z_0}^{z_N}\psi_n(z)f dz. \tag{12}$$

$\psi_{(m)}$ and $\psi_{(n)}$ define respectively the m-th and n-th spatial trial functions. Rearranging this expression by bringing the right-hand side to the left yields:

$$\int_{z_0}^{z_N} dz\left[(\rho\omega^2 - k_x^2\mu - k_y^2\mu)\sum_m c_m\psi_m(z) + \frac{\partial}{\partial z}\left(\mu\frac{\partial}{\partial z}\sum_m c_m\psi_m(z)\right) + f\right]\psi_n(z) = 0 \tag{13}$$

The weak form of the equation of motion can be rewritten into the discretised spatial components by simplification of eq. 13 using the following expressions for the unmodified matrix and vector elements for the SH problem.

$$g_m = \int_{z_0}^{z_N} \psi_m f dz \tag{14}$$

$$T_{mn} = \int_{z_0}^{z_N} \psi_m \rho \psi_n dz \tag{15}$$

and

$$H_{mn} = (k_x + k_y)^2 H_{mn}^{(1)} + H_{mn}^{(2)} \tag{16}$$

with,

$$H_{mn}^{(1)} = \int_{z_0}^{z_N} \psi_m \mu \psi_n dz \tag{17}$$

$$H_{mn}^{(2)} = \int_{z_0}^{z_N} \psi_m^{'} \mu \psi_n^{'} dz \tag{18}$$

into,

$$(\omega^2 \mathbf{T} - \mathbf{H})\mathbf{c} = -\mathbf{g} \tag{19}$$

Eq. 19 describes the Galerkin weak form for solving the equation of motion known as the Direct Solution Method (DSM), where **T** is the mass matrix, **H** the stiffness matrix, **g** defines the force vector and **c** is the eigenvector. Prime's in the superscript denote partial derivatives in space z. This formulation adheres to free surface boundary conditions, and further coverage of boundary conditions is not discussed in this paper.

2.4 Trial Functions

The general matrix expression in eq. 19 for the equation of motion is suitable for both an FDM and FEM approach, depending on the shape of the function which are arbitrarily chosen for trial functions ψ_m and ψ_n. Finite difference operators are obtained if the trial functions are taken as a linear spline function. The solution to equation eq. 19 is exact only if trial functions ψ_m and ψ_n are infinite in number. Hence, errors in the numerical schemes originate due to truncation of the trial functions. The error will vary depending on the shape function chosen for the trial functions in eq. 11 , being a linear spline function ψ_m^{lin} or a sinc function ψ_m^{sinc}.

$$u^{lin} = \sum_{m}^{N} c_m^{lin} \psi_m^{lin} \quad (m = 0, ..., N) \tag{20}$$

$$u^{sinc} = \sum_{m}^{N} c_m^{sinc} \psi_m^{sinc} \quad (m = 0, ..., N) \tag{21}$$

$$\psi_m^{sinc} = \psi_m^{lin} + E\psi_m^{lin} \quad (E \neq 0) \tag{22}$$

where the function E represents the difference between the shape functions. However, the operators in eq. 15 and eq. 16 are not exact, but contain an error due to the truncation of either of these trial functions.

$$\mathbf{T} = \mathbf{T}^{\mathbf{exact}} + \delta\mathbf{T} \tag{23}$$

$$\mathbf{H} = \mathbf{H}^{\mathbf{exact}} + \delta\mathbf{H} \tag{24}$$

$$\mathbf{c} = \mathbf{c}^{\mathbf{exact}} + \delta\mathbf{c} \tag{25}$$

The exact operators are denoted by $\mathbf{T}^{\mathbf{exact}}$ and $\mathbf{H}^{\mathbf{exact}}$, and the exact solution by $\mathbf{c}^{\mathbf{exact}}$. The error of the numerical operators are defined by $\delta\mathbf{T}$ and $\delta\mathbf{H}$, whereas the error of the numerical solution is given by $\delta\mathbf{c}$. Since the error of the numerical solution changes depending on the shape of the trial function, the error to the numerical solution can be written by subtracting the solution of the sinc case from the linear case:

$$\delta\mathbf{c} = \mathbf{c}^{lin} - \mathbf{c}^{sinc} \tag{26}$$

where $\mathbf{c}^{lin}$ and $\mathbf{c}^{sinc}$ are the solutions to the eigenvectors of respectively the linear and the sinc interpolation.

2.5 Normal mode basis analysis

To discuss the spatial dependence of the operators we consider eq. 19 for a single point M in time.

$$(\omega_M^2\mathbf{T} - \mathbf{H})\mathbf{c}_M = -\mathbf{g}_M. \tag{27}$$

The exact solution, the numerical solution and its errors are represented by eigenfunction expressions as in [Geller and Takeuchi, 1995]. The numerical values of the eigenvalues and eigenvectors are not required to be known. We represent the normal modes as following:

$$(\omega_{\mathcal{M}}^2\mathbf{T}^{\text{exact}} - \mathbf{H}^{\text{exact}})\mathbf{d}_{\mathcal{M}} = 0. \tag{28}$$

Here, $\omega_{\mathcal{M}}$ is the eigenfrequency of the m-th mode, $\mathbf{d}_{\mathcal{M}}$ is ortho-normalized eigenvector. The mass and stiffness matrices are the exact operators rather than the conventional ones. Equation 28 can be rewritten as follows:

$$\mathbf{d}_{\mathcal{M}}^*\mathbf{H}^{\text{exact}}\mathbf{d}_{\mathcal{N}} = \omega_{\mathcal{M}}^2\mathbf{d}_{\mathcal{M}}^*\mathbf{T}^{\text{exact}}\mathbf{d}_{\mathcal{N}} = \omega_{\mathcal{M}}^2\delta_{\mathcal{M}\mathcal{N}} \tag{29}$$

with $\delta_{\mathcal{M}\mathcal{N}}$ being a Kronecker delta. Using an eigenfunction expansion for eq. 29, we obtain the following expression that the exact operators must satisfy:

$$\mathbf{d}_{\mathcal{M}}^*(\omega_{\mathcal{M}}^2\mathbf{T}^{\text{exact}} - \mathbf{H}^{\text{exact}})\mathbf{d}_{\mathcal{M}} = 0. \tag{30}$$

For a one-dimensional medium the normal mode can be written as the sum of the spatial trial functions as in eq. 11, in which case the exact operators in eq. 29 should satisfy:

$$\begin{aligned}
& \mathbf{d}_{\mathcal{M}}^*(\omega_{\mathcal{M}}^2\mathbf{T}^{\text{exact}} - \mathbf{H}^{\text{exact}})\mathbf{d}_{\mathcal{M}} \\
= & \sum_m d_{n\mathcal{M}}^* \left[\omega_{\mathcal{M}}^2 \int_z \psi_{m*}\rho u^{\mathcal{M}} dz - \int_z \psi_{m*}\mu^{\mathcal{M}} u^{\mathcal{M}'}\, dz\right] \\
= & \ \omega_{\mathcal{M}}^2 \int_z u^{\mathcal{M}*}\rho u^{\mathcal{M}} dz - \int_z u^{\mathcal{M}*}\mu^{\mathcal{M}} u^{\mathcal{M}'} dz \\
= & \ 0
\end{aligned} \tag{31}$$

2.6 Cartesian regular grid

The computational grid is described by a Cartesian coordinate system with N gridpoints. We consider only localized spatial trial functions for a receiver point $\mathbf{r}_n$:

$$\psi_m(\mathbf{r}_n) = \delta_{mn} \tag{32}$$

and

$$\exists\alpha > 0; \forall|\mathbf{r} - \mathbf{r}_n| > \alpha; \phi_m(\mathbf{r}) = 0 \tag{33}$$

for discretized nodes the receiver points are written as:

$$(\mathbf{r}_n) = z_n \tag{34}$$

$$z_n = z_0 + n\Delta z \tag{35}$$

where Δz denotes the grid spacing and $\mathbf{r}_0$ the starting point. This theory can be generalised to a set of spatial trial functions that have sensitivities in several nodes.

The localised trial function ψ can be rewritten as a product of one-dimensional localised trial functions:

$$\psi_m(\mathbf{r}) = \prod_{k=1}^{\mathfrak{N}} X_k^{(m_k)} \tag{36}$$

with

$$X^{(m)}(z_n) = \delta_{mn} \tag{37}$$

and

$$X^{(m)}(z) = 0 \quad \text{for} \quad |z - z_m| > l\Delta z \tag{38}$$

where $2l + 1$ is the number of nodes that contain non-zero values in the operators. Truncation of the trial functions at the boundary nodes will be satisfied through the application of natural boundary conditions.

2.7 Optimally Accurate 1D SH operators

For the optimal case the Galerkin weak form of the equation of motion will look as in eq. 39. Instead of expressing the displacement as a summation of the trial functions and the eigenvector in point m, we rewrite it as an infinite Taylor series expansion, which can be expanded to get eq. 40. Here l denotes the number of nodes in the forward/backward difference stencil (l=0 in boundary nodes). The operators are determined for $l \leq m \leq N - l$.

$$\sum_{n=m-l}^{m+l} (\omega^2 T_{mn}^{opt} - H_{mn}^{opt}) \sum_{h=0}^{\infty} \frac{u_{(m\Delta z)}^h}{h!} (n\Delta z)^h \tag{39}$$

$$= \sum_{n=m-l}^{m+l} (\omega^2 T_{mn}^{opt} - H_{mn}^{opt})[u_{(m\Delta z)} + (n\Delta z)u'_{(m\Delta z)} + \frac{(n\Delta z)^2}{2} u''_{(m\Delta z)} + \frac{(n\Delta z)^3}{6} u'''_{(m\Delta z)} + \frac{(n\Delta z)^4}{24} u''''_{(m\Delta z)} + \mathbf{O}(\Delta z)^5] \tag{40}$$

Expanding eq. 40 by multiplying the Taylor series with the individual operators $\mathbf{T}$ and $\mathbf{H}$ gives the following expression.

$$= \sum_{n=m-l}^{m+l} [\omega^2 T_{mn} u_{(m\Delta z)} + \omega^2 T_{mn}(n\Delta z) u'_{(m\Delta z)} + \omega^2 T_{mn} \frac{(n\Delta z)^2}{2} u''_{(m\Delta z)} + \dots]$$
$$- \sum_{n=m-l}^{m+l} [\omega^2 H_{mn} u_{(m\Delta z)} + \omega^2 H_{mn}(n\Delta z) u'_{(m\Delta z)} + \omega^2 H_{mn} \frac{(n\Delta z)^2}{2} u''_{(m\Delta z)} + \dots] \quad (41)$$

For each order of derivation for u in the above expression we evaluate the value of the operators according to eq. 15 and eq. 16. Using Fig. 1a and Fig. 1b which display the values of the trial functions and its derivative in a central node m these expressions can be verified. For a 0th order derivative $u_{(m\Delta z)}$, the operators $\mathbf{T}$ and $\mathbf{H}$ look as following,

$$\sum_{n=m-l}^{m+l} \omega^2 T_{mn} = \omega^2 \int_{z_0}^{z_N} \psi_m \rho dz \quad (42)$$

$$\sum_{n=m-l}^{m+l} \omega^2 H_{mn} = 0 \quad (43)$$

The 1st order derivative $u'_{(m\Delta z)}$ for the operators yield:

$$\sum_{n=m-l}^{m+l} \omega^2 T_{mn}(n\Delta z) = 0 \quad (44)$$

$$\sum_{n=m-l}^{m+l} \omega^2 H_{mn}(n\Delta z) = -\int_{z_0}^{z_N} \psi_m \mu dz \quad (45)$$

And for the 2nd order derivative $u''_{(m\Delta z)}$ the results are:

$$\sum_{n=m-l}^{m+l} \omega^2 T_{mn} \frac{(n\Delta z)^2}{2} = 0 \quad (46)$$

$$\sum_{n=m-l}^{m+l} \omega^2 H_{mn} \frac{(n\Delta z)^2}{2} = -\int_{z_0}^{z_N} \psi_m \mu dz \quad (47)$$

By substituting these expressions into eq. 41 we can obtain the ideal operators as function of the trial function ψ_m and displacement u.

$$\mathbf{H}^{exact}(\psi_m, u) = \psi_m \mu u'|_{discon} - \int_{z_0}^{z_N} \psi_m (\mu u')' dz \quad (48)$$

$$\mathbf{T}^{exact}(\psi_m, u)_m = \int_{z_0}^{z_N} \psi_m \rho u dz \quad (49)$$

Eq. 48 contains a discontinuity term which is only relevant for boundary nodes, which we do not treat in this paper. Equations 48 and 49 must be evaluated only for $u^h_{(m\Delta z)}$ to obtain the optimised operators for the one-dimensional SH case.

$$
\begin{aligned}
[\omega^2 T^{exact}_{mn} - H^{exact}_{mn}]\mathbf{u} = \omega^2 \int_{z_0}^{z_N} \psi_m \rho \sum_{h=0}^{\infty} \frac{u^h_{(m\Delta z)}}{h!}(z - m\Delta z)^h dz \\
- \psi_m \mu_{(z_N)} u^{'}_{(z_N)} + \psi_m \mu_{(z0)} u^{'}_{(z_0)} \\
+ \int_{z_0}^{z_N} \psi_m \mu \sum_{h=2}^{\infty} \frac{u^h_{(m\Delta z)}}{h!} h(h-1)(z - m\Delta z)^{h-2} dz \\
+ \int_{z_0}^{z_N} \psi_m \mu^{'} \sum_{h=1}^{\infty} \frac{u^h_{(m\Delta z)}}{h!} h(z - m\Delta z)^{h-1} dz
\end{aligned} \tag{50}
$$

$$
\begin{aligned}
= \Big[\omega^2 \int_{z_0}^{z_N} \psi_m \rho u_{(m\Delta z)} dz + \omega^2 \int_{z_0}^{z_N} \psi_m \rho u^{'}_{(m\Delta z)} \Big(\frac{z}{\Delta z} - m\Big)\Delta z dz \\
+ \omega^2 \int_{z_0}^{z_N} \psi_m \rho u^{''}_{(m\Delta z)} \Big(\frac{z}{\Delta z} - m\Big)^2 \frac{\Delta z^2}{2} dz + \dots \Big] \\
- \psi_m \mu_{(z_N)} u^{'}_{(z_N)} + \psi_m \mu_{(z0)} u^{'}_{(z_0)} \\
+ \Big[\int_{z_0}^{z_N} \psi_m \mu u^{''}_{(m\Delta z)} dz + \int_{z_0}^{z_N} \psi_m \mu u^{'''}_{(m\Delta z)} \Big(\frac{z}{\Delta z} - m\Big)\Delta z dz \\
+ \int_{z_0}^{z_N} \psi_m \mu^{'} u^{''''}_{(m\Delta z)} \Big(\frac{z}{\Delta z} - m\Big)^2 \frac{\Delta z^2}{2} dz + \dots \Big] \\
+ \Big[\int_{z_0}^{z_N} \psi_m \mu^{'} u^{'}_{(m\Delta z)} dz + \int_{z_0}^{z_N} \psi_m \mu^{'} u^{''}_{(m\Delta z)} \Big(\frac{z}{\Delta z} - m\Big)\Delta z dz \\
+ \int_{z_0}^{z_N} \psi_m \mu^{'} u^{'''}_{(m\Delta z)} \Big(\frac{z}{\Delta z} - m\Big)^2 \frac{\Delta z^2}{2} dz + \dots \Big]
\end{aligned} \tag{51}
$$

Eq. 51 can be simplified to give the optimised operator to a second order of accuracy, displayed below.

$$
[\omega^2 T^{exact}_{mn} - H^{exact}_{mn}]\mathbf{u} = \omega^2 \int_{z_0}^{z_N} \psi_m \rho u_{(m\Delta z)} dz + \int_{z_0}^{z_N} \psi_m \mu u^{''}_{(m\Delta z)} dz + \int_{z_0}^{z_N} \psi_m \mu^{'} u^{'}_{(m\Delta z)} dz \tag{52}
$$

3 Impact of trial functions on seismic modelling

The solutions to the Galerkin weak form of the equation of motion only requires the continuity of displacement to be explicitly satisfied. Boundary conditions involving traction are treated as natural boundary conditions, which are completely satisfied by a complete set of trial functions. However, since the computational domain consists of a grid the set of trial functions is not complete, obtaining only an approximation to the solution [Geller and Hatori, 1995]. Truncation of the trial functions between the grid points causes numerical dispersion, producing errors in the solution. Only when the trial function expansion used for grid interpolation is infinite and

incorporates infinitesimally small grid spacing, then an exact solution will be reached. Since these conditions are computationally unattainable, we require optimisation of the operators to accommodate the truncation error.

The trial function of choice for the interpolation of the computational grid is arbitrary, on the premise that the weighting of the elastic parameters is stable along the entire grid. According to equations 15 and 16 stability is governed by the product of the m-th and n-th trial function, which must produce a constant value of 1 for ρ and μ to be stable along the grid.

3.1 Finite Difference Method

When using a Finite Element Method with a linear grid interpolation of the nodes as the basis of the trail functions we speak of the Finite Difference Method. Use of FDM has had an increased popularity within exploration geophysics for the modelling of seismic waveforms. FD numerical schemes are able to handle fairly complex geological models and produce relatively accurate results, whereas computationally it is comparatively efficient. The balanced tradeoff between accuracy and efficiency make it a suitable method to suppress costs while attaining sufficient resolution to meet target criteria [Moczo et al., 2007].

With FD modelling of seismic wave propagation the computational domain consists of a conventional uniform Cartesian space-time grid, where the functions describing the wavefield and material properties are contained in the nodal points of the non-staggered grid. At any given grid position the spatial and time derivatives of these functions are approximated by FD expressions through a system of algebraic equations using function values of neighbouring grid points through Taylor expansions [Moczo et al., 2007]. For a scheme considering only the direct neighbours, a three-point scheme, the first derivative of a continuous displacement function $u(z)$ can be approximated by the forward, backward and central difference relations between the nodes.

$$\frac{\partial u(z_0)}{\partial z} \approx \frac{u(z_0 + \Delta z) - u(z_0)}{\Delta z} \tag{53}$$

$$\frac{\partial u(z_0)}{\partial z} \approx \frac{u(z_0) - u(z_0 - \Delta z)}{\Delta z} \tag{54}$$

$$\frac{\partial u(z_0)}{\partial z} \approx \frac{u(z_0 + \Delta z) - u(z_0 - \Delta z)}{2\Delta z} \tag{55}$$

Here z_0 describes the central node in question, and Δz the grid spacing between the nodes. We express the forward and backward functional values $u(z_0 + \Delta z)$ and $u(z_0 - \Delta z)$ as their respective Taylor expansions about point z_0:

$$u(z_0 + \Delta z) = u(z_0) + \Delta z\Big(\frac{\partial u(z_0)}{\partial z}\Big) + \frac{(\Delta z)^2}{2}\Big(\frac{\partial^2 u(z_0)}{\partial z^2}\Big) + \frac{(\Delta z)^3}{6}\Big(\frac{\partial^3 u(z_0)}{\partial z^3}\Big) + \dots \tag{56}$$

$$u(z_0 - \Delta z) = u(z_0) - \Delta z\Big(\frac{\partial u(z_0)}{\partial z}\Big) + \frac{(\Delta z)^2}{2}\Big(\frac{\partial^2 u(z_0)}{\partial z^2}\Big) - \frac{(\Delta z)^3}{6}\Big(\frac{\partial^3 u(z_0)}{\partial z^3}\Big) + \dots \tag{57}$$

Rearranging these expressions to solve for the first derivative of the displacement will give us a first approximation truncation error (red) for the forward and backward operators proportional to grid spacing Δz,

$$\frac{\partial u(z_0)}{\partial z} = \frac{u(z_0+\Delta z)-u(z_0)}{\Delta z} - \frac{\Delta z}{2}\left(\frac{\partial^2 u(z_0)}{\partial z^2}\right) - \frac{(\Delta z)^2}{6}\left(\frac{\partial^3 u(z_0)}{\partial z^3}\right) + \dots \tag{58}$$

$$\frac{\partial u(z_0)}{\partial z} = \frac{u(z_0)-(z_0-\Delta z)}{\Delta z} + \frac{\Delta z}{2}\left(\frac{\partial^2 u(z_0)}{\partial z^2}\right) - \frac{(\Delta z)^2}{6}\left(\frac{\partial^3 u(z_0)}{\partial z^3}\right) + \dots \tag{59}$$

and a second approximation for the central difference operator with truncation error proportional to Δz^2,

$$\frac{\partial u(z_0)}{\partial z} = \frac{u(z_0+\Delta z)-u(z_0-\Delta z)}{2\Delta z} - \frac{(\Delta z)^2}{6}\left(\frac{\partial^3 u(z_0)}{\partial z^3}\right) + \dots \tag{60}$$

These equations describe the solution to a conventional Finite Difference approach. During the process of full waveform inversion using the conventional method truncation errors will propagate through the solution, inflating for each iteration of the inversion. Therefore it is imminent to modify the mass matrix **T** and stiffness matrix **H** to become optimally accurate to maintain accuracy during the inversion process.

For a three point difference scheme a linear spline interpolation meets these criteria for solving the mass matrix **T**, since the sum of the area between the spline functions remains 1 throughout the grid (Fig. 2). However, numerically solving for the stiffness matrix **H** will produce a slight error because the derivative of a triangle function is non-existent in its peak and will therefore not produce an output for the central node (Fig. 1a). This error is proportional to the spacing of the points used to interpolate the trial function, and can be diminished by increasing the number of points to describe the function in return for additional computation time. The linear spline interpolation is only suitable for a three-point scheme since when used for higher order difference schemes too much weight is given to the direct neighbouring nodes. To counter this imbalance an additional correction term is required to stabilise the elastic parameters for each increasing order of the difference scheme, costing unnecessary computation time. The linear spline function therefore doesn't hold up for higher order difference schemes, which is why it is favourable to revisit the possibilities for the shape function used for grid interpolation of higher order difference schemes.

3.2 Sinc Trial Function for FEM

The proposed trial function to be used for higher order difference schemes in this paper is a *sinc*-function (Fig. 1c to Fig. 1f).

$$sinc(\pi x_i) = \frac{sin(\pi x_i)}{\pi x_i} \tag{61}$$

The properties of this function that make it suitable for higher order schemes, additionally to being differentiable in each point, is the repeating nature of the *sinc*-function for every cycle of π. Regardless of the number of points in the scheme, the *sinc*-function equals to zero in each of the neighbouring nodal points, whereas in between the nodes the sidelobes of the trial functions sum to effectively negate each other to approach a constant weighting of 1 along the grid (Fig. 4). The only exception to this is for a three-point scheme, where the *sinc*-function is incomplete and instead closely resembles a non-linear spline, causing the weighting of the elastic parameters to fluctuate in between the nodal points (Fig. 3). Thus, for a three-point difference scheme the linear interpolation remains superior. However, one could argue that in order to realistically model wave propagation neither the linear spline function nor a *sinc*-function for a

three-point system adequately represents the particle motion of a waveform, which could make a slight difference for heterogenous media. Both for more realistic grid interpolation and improved reduction of the truncation error, we propose to use a five-point *sinc* interpolation for waveform generation.

At a single node m the weighting of the elastic parameters for the forward and backward difference is decided by the overlap between the m-th and n-th trial function. A weight distribution of the elastic parameters about m is represented by an array (1D) or matrix (2D) containing coefficients for each possible overlap scenario as the n-th trial function is shifted along m. The summation of these arrays, or matrices, along the entire grid will equal to 1.

For any given shape function in a three-point system there are only three possible overlap scenarios per cardinal direction, as shown in Fig. 2 and Fig. 3 for the one-dimensional case, and Fig. 5 for two dimensions. The weight distribution around point m for one-dimension is therefore described by a one-by-three array, and for the two-dimensional case by a three-by-three matrix. For higher order difference schemes the number of overlap scenarios increases at double the rate than that of the number of points in the scheme. A five-point difference scheme, for example, gives seven trial function overlap possibilities in each cardinal direction as is shown in Fig. 4 and Fig. 6, giving a weight distribution in the form of a seven point array or a seven-by-seven matrix. Going further, a seven-point scheme would provide eleven overlap scenarios. The increase in grid coverage per difference scheme means that as we increase the order of the difference scheme, heterogeneities along the grid will be accommodated better during the computation of the displacement for a single node m.

Given a one-dimensional overlap scheme (either three- or five-point) between the trial functions we obtain each individual weight coefficient for the mass matrix $\mathbf{T}$ and stiffness matrix $\mathbf{H}^1$ for each possible combination of the m-th and n-th position, as shown in equations 15 and 17. The same scheme for the 1-st order derivative of the trial function gives us the coefficients for stiffness matrix $\mathbf{H}^2$ as shown in equation . In the two-dimensional space another set of trial functions is introduced for the direction orthogonal to the primary axis. For an overlap stencil where all trial functions in the x and z orientation are derivatives of the 0-th order, we obtain the following two-dimensional expression for mass matrix T.

$$T_{mn} = \int_{m=0}^{N} dV \rho(x,z) \left(\psi_x^{(mx,mz)} \psi_z^{(mx,mz)}\right) \left(\psi_x^{(nx,nz)} \psi_z^{(nx,nz)}\right) \tag{62}$$

Multi-directional variety in the combination of the 0-th and 1-st order trial function derivatives in the x and z direction result in four different components of the stiffness matrix, H^{11}, H^{33}, H^{13} and H^{31}, where the numerals 1 and 3 denote respectively the x and z orientation.

$$\mathbf{H^{11}} = \int_{m=0}^{N} dV C_{xxxx} \left(\left[\frac{\partial}{\partial x} \psi_x^{(mx,mz)} \right] \psi_z^{(mx.mz)} \right) \cdot \left(\left[\frac{\partial}{\partial x} \psi_x^{(nx,nz)} \right] \psi_z^{(nx,nz)} \right) \tag{63}$$

$$\mathbf{H^{33}} = \int_{m=0}^{N} dV C_{zzzz} \left(\psi_x^{(mx,mz)} \left[\frac{\partial}{\partial z} \psi_z^{(mx.mz)} \right] \right) \cdot \left(\psi_x^{(nx,nz)} \left[\frac{\partial}{\partial z} \psi_z^{(nx,nz)} \right] \right) \tag{64}$$

$$\mathbf{H^{13}} = \int_{m=0}^{N} dV C_{xxzz} \left(\left[\frac{\partial}{\partial x} \psi_x^{(mx,mz)} \right] \psi_z^{(mx.mz)} \right) \cdot \left(\psi_x^{(nx,nz)} \left[\frac{\partial}{\partial z} \psi_z^{(nx,nz)} \right] \right) \tag{65}$$

$$\mathbf{H^{31}} = \int_{m=0}^{N} dV C_{zzxx} \left(\psi_x^{(mx,mz)} \left[\frac{\partial}{\partial z} \psi_z^{(mx.mz)} \right] \right) \cdot \left(\left[\frac{\partial}{\partial x} \psi_x^{(nx,nz)} \right] \psi_z^{(nx,nz)} \right) \tag{66}$$

4 Numerical examples

4.1 Trial function coefficients

In tables 1 to 21 we present the coefficients related to the contribution of the trial functions for the mass matrix **T** and the stiffness matrix **H**, for the different trial functions, difference schemes and spatial dimensions. The benchmark results for a one-dimensional three-point spline, as shown in [Geller and Takeuchi, 1995], are presented in tables 1 and 2. Here the position of the m-th trial function along a grid with five points is displayed vertically, whereas the position of the n-th trial function is shown horizontally, as the wave displaces through time from the first to the fifth node in a homogeneous medium. The results for the same case using sinc trial function are shown in table 3 and 4. For a one-dimensional five-point difference scheme using a sinc function the results are shown in table 5 and 6, and only display the coefficients for one node in a system rather than a grid of five nodes. This format will from here on be used for the remainder of the result tables. The two-dimensional case is treated in tables 7 to 21, where tables 7 to 11 show the results for a three-point spline function, tables 12 to 16 for a three-point sinc function, and tables 17 to 21 for a five-point sinc function.

4.2 2D synthetic waveforms

Two dimensional synthetic waveforms were generated for a homogeneous medium, using the conventional and optimised operators as shown in respectively Fig. 12 and Fig. 13. Frechet sensitivity kernels are displayed in Fig. 14 and Fig. 15, generated for both the conventional and optimised operators for elastic wave propagation.

5 Discussion

To establish a benchmark for the validation of the data tables for the weighting coefficient arrays and matrices in the result section we used the results of the 1D homogeneous SH case from Geller and Takeuchi 1995. Reproducing the results for the bulk of their mass and stiffness matrices plus the surface boundary conditions, as shown in tables 1 and 2, we can verify that the main motor of the code works as expected. The table presents the overlap coefficients between two splines for each node between 1 and 5. The boundary nodes only receive half the contribution of the overlapping trial function, resulting in half the weight value for these nodes. Only the $\mathbf{H}^{(2)}$ boundary nodes display a slight deviation of 0.02 from the result of Geller & Takeuchi 1995, which is because there is no 1st derivative of the spline function in the central node. The function is interpolated using 100 points for Δz, and the trial function ranges from $(z_0 - \Delta z)$ to $(z_0 + \Delta z)$, giving 200 points for the interpolation of a three-point trial function. However, the spline function is computed in two steps, separated into the ascending and descending part of the function, meaning there are two points which describe the central node, for which there is no derivative. Each point accounts for 1/100th of the weight coefficient, hence the deviation of 0.02 for both points. It was decided to leave the code unaltered since the focus of the study was with the sinc trial functions, and since these are differentiable in each point it would not result into an error for sinc functions. From this we conclude that the values for the three-point sinc function presented in Fig. 3 and Fig. 4 are correct. The values are higher than their linear spline counterparts, since although closely resembling a linear spline as seen in Fig.1c, its rounded features cause it to have a higher area than the spline function. Eventhough at the nodal points the contributions of the m-th and the n-th trial function is 1 and 0 that sum to a stable value of 1 at each grid point, exactly halfway in between the grid points the value of both functions is slightly higher than 0.5. The joint contribution of the sinc trial functions to the elastic parameters in between the nodes is therefore greater than 1 (Fig. 3), meaning the

elastic parameters are not constant along the grid for this case. Using a sinc interpolation for a three-point difference scheme is therefore not accurate. However, verification of the values for this case was valuable to guarantee proper functioning of the motor of the code. By expanding the algorithm it allows for the computation of the weight coefficients for sinc functions in higher order difference schemes. Spline functions for higher order schemes are not a viable option, because the contribution of a linear spline function across two nodes will double the weighting coefficients in each node. The trial function needs a negative contribution to avoid inflation of the elastic parameters. Fig.4 shows that for a five-point sinc function the sum of the trial functions is not precisely stable around the value 1. Due to a slight asymmetry in the side lobes of the sinc function there is a slight fluctuation of the stability, which converges to 0 as the order of the difference scheme increases. This means the viability of a sinc function for grid interpolation improves as the order of the scheme increases.

From the data tables it is possible to quantify the instability from the trial functions upon the elastic parameters, by summing the coefficients in the matrices. To obtain stable operators the weight coefficients for the mass matrix T should sum to a value of 1, which is confirmed by the results for one- and two-dimensional spline functions for a three point difference scheme in tables 1 and 7. For the three-point sinc case it is already known the trial functions do not provide a stable weight distribution, which is verified by tables 3 and 12. The one-dimensional case inflates the elastic parameters by roughly a factor 1.4, and in two dimensions this increases to approximately 2. It shows a strong propagation of the instability of the trial function in the solution as the model dimensions increase. For a three-dimensional wave propagation model the weight coefficients for the elastic parameters would have a projected increase of a factor 2.8, nearly three times the desired value. This strong effect is similarly observed in the case of a five-point sinc function. Addition of the two negative sidelobes to the scheme has resulted in the sum of the coefficients for the mass matrix to fall slightly below 1 instead (0,8172), which means an underrepresentation of the elastic parameters. For a two dimensional case this would mean a decrease to roughly two-thirds (0,668) of the actual coefficient value, and estimated half the value for a three-dimensional space. The numerical examples show a high sensitivity of the stability of the trial functions to the numerical solution, and the importance of stable trial functions especially as we work towards a three-dimensional model. Although the deviation of the weight coefficients reduces with increasing order of the difference scheme, the results show that sinc trial functions for a five-point scheme have too large of an error margin.

However, as the order of the difference scheme increases by one node on either side, the number possibilities in which the trial functions can overlap increases by double of that. For example, a five-point difference scheme in a one-dimensional system (Fig.4) shows 7 overlap scenarios for the trial functions, which are 4 more possibilities than that of a three-point difference scheme. The reason is because the difference scheme gains an additional off-centre forward and backward difference operator per expansion of the points used in the system. In the five-point case the forward difference formula incorporates the nodes from $(z_0 - \Delta z)$ to $(z_0 + 3\Delta z)$, whereas the backward difference formula from $(z_0 - 3\Delta z)$ to $(z_0 + \Delta z)$. Therefore the nodes at $(z_0 - 3\Delta z)$ and $(z_0 + 3\Delta z)$ have a single overlap situation contributing to the stability of the elastic parameters, despite being outside the influence of the central difference operator. The increase in grid coverage for each higher order of the difference scheme has an exponential effect as we add extra dimensions to our model, which is apparent through a comparison between the three-point and five-point overlap figures in the two-dimensional space (Fig.5 and Fig.6) with respect to one dimension. It shows that as we move from a three-point system to a five point system for a 2D-case, there is an increase from 9 to 49 overlap scenarios, which is rather significant compared to an increase from 3 to 7 for the 1D-case. If we would use a five-point difference stencil for synthetic wave propagation for a hypothetical three-dimensional case, there would be a total of 343 overlap possibilities for the trial functions compared to 49 scenarios for a three-point

scheme. That is 343 coefficients to express the weighting of the elastic parameters for the mass matrix **T** and stiffness matrices **H** for a grid point m. For heterogenous media that means that the coefficients in **H** are a function of the shear modulus μ in point m and n, as the elastic modulus is anisotropic. The solution for the weak form of the equation of motion for a five-point difference scheme will therefore accommodate heterogeneity much better than a three-point scheme because the grid coverage for the assessment of a nodal point m gets exponentially larger for each dimensional space.

Regardless of the difference scheme used for synthetic waveform generation, the method remains based on approximations of the partial differential equations and will contain numerical errors. Optimisation of the spatial and temporal operators to obtain the exact mass and stiffness matrices is encouraged in order to reduce numerical dispersion from the synthetic waveforms. Figures 12 and 13 compare 2D synthetic waveforms using the conventional and optimal operators for a homogenous medium. There is clear ringing behind the ray fronts in figure 12, caused by the numerical dispersion from approximating the solution. Using the optimised operators as in figure 13, it is shown that the ringing is greatly reduced. The Frechet kernels in figures 14 and 15 show a more localised sensitivity when using optimised operators. Especially for layered model structures there is increased interference of numerical errors with the waveform that cause artefacts within the synthetic waveforms.

6 Conclusion

The results highlight the importance of stable trial functions to accurately describe the elastic parameters along the grid for the operators of wave propagation. High sensitivity to deviations will cause fluctuations in the weight coefficients when summed for the grid which amplify for each dimension added to the computational space. Therefore using sinc trial functions for grid interpolation becomes less feasible for synthetic wave generation for the two- and three-dimensional cases. Perspectives for sinc trial function remain within one-dimensional wave propagation models for higher order schemes, where the sum of the coefficients converges to 0 and acceptable stability is acquired.

Although the use of Sinc trial functions for grid interpolation provides adequate stability for a limited number of cases, it remains of interest to quantify the effect of using waveform-like trial functions compared to linear splines. Further potential research could involve higher order 1D difference schemes for synthetic waveform generation, where a stable sinc interpolation is compared with a linear spline approach for the modeling of more complex, "real Earth" scenarios.

7 Acknowledgments

Hereby I would like to express my gratitude to N. Fuji for granting me this opportunity to learn about the intricacies of numerical modelling and guiding me through this research project as my supervisor from IPGP. Secondly, I would like to thank H. Paulssen for taking it upon her to be my supervisor from the University of Utrecht and for following my progress during this research project.

References

Keiiti Aki and Paul G Richards. *Quantitative seismology*, volume 1. Published by University Science Books, 2002.

Robert J. Geller and Tomohiko Hatori. DSM synthetic seismograms using analytic trial functions: plane-layered, isotropic, case. *Geophysical Journal International*, 120:163–172, 1995.

Robert J. Geller and Nozomu Takeuchi. A new method for computing highly accurate DSM synthetic seismograms. *Geophysical Journal International*, 123:449–470, 1995.

Robert J. Geller and Nozomu Takeuchi. Optimally accurate second-order time-domain finite difference scheme for the elastic equation of motion: one-dimensional case. *Geophysical Journal International*, 135:48–62, 1998.

Martin Käser and Michael Dumbser. An arbitrary high-order discontinuous galerkin method for elastic waves on unstructured meshes part 1. The two-dimensional isotropic case with external source terms. *Geophysical Journal International*, 166(2):855–877, 2006.

Dimitri Komatitsch and Jean-Pierre Vilotte. The spectral element method: An efficient tool to simulate the seismic response of 2d and 3d geological structures. *Bulletin of the Seismological Society of America*, 88:368–392, 1998.

Peter Moczo, Johan Robertsson, and Leo Eisner. The finite-difference time-domain method for modeling of seismic wave propagation. *Elsevier*, 48:421–516, 2007.

R-E Plessix. A review of the adjoint-state method for computing the gradient of a functional with geophysical applications. *Geophysical Journal International*, 167(2):495–503, 2006.

Gilbert Strang and George Fix. *An Analysis of the Finite Element Method*, volume 2. Published by University Science Books, 1973.

C. Thurber and J. Ritsema. Theory and observations. Seismic tomography and inverse methods. *Elsevier*, 2007.

Jeroen Tromp, Carl Tape, and Qinya Liu. Seismic tomography, adjoint methods, time reversal and banana-doughnut kernels. *Geophysical Journal International*, 160:195–216, 2005.

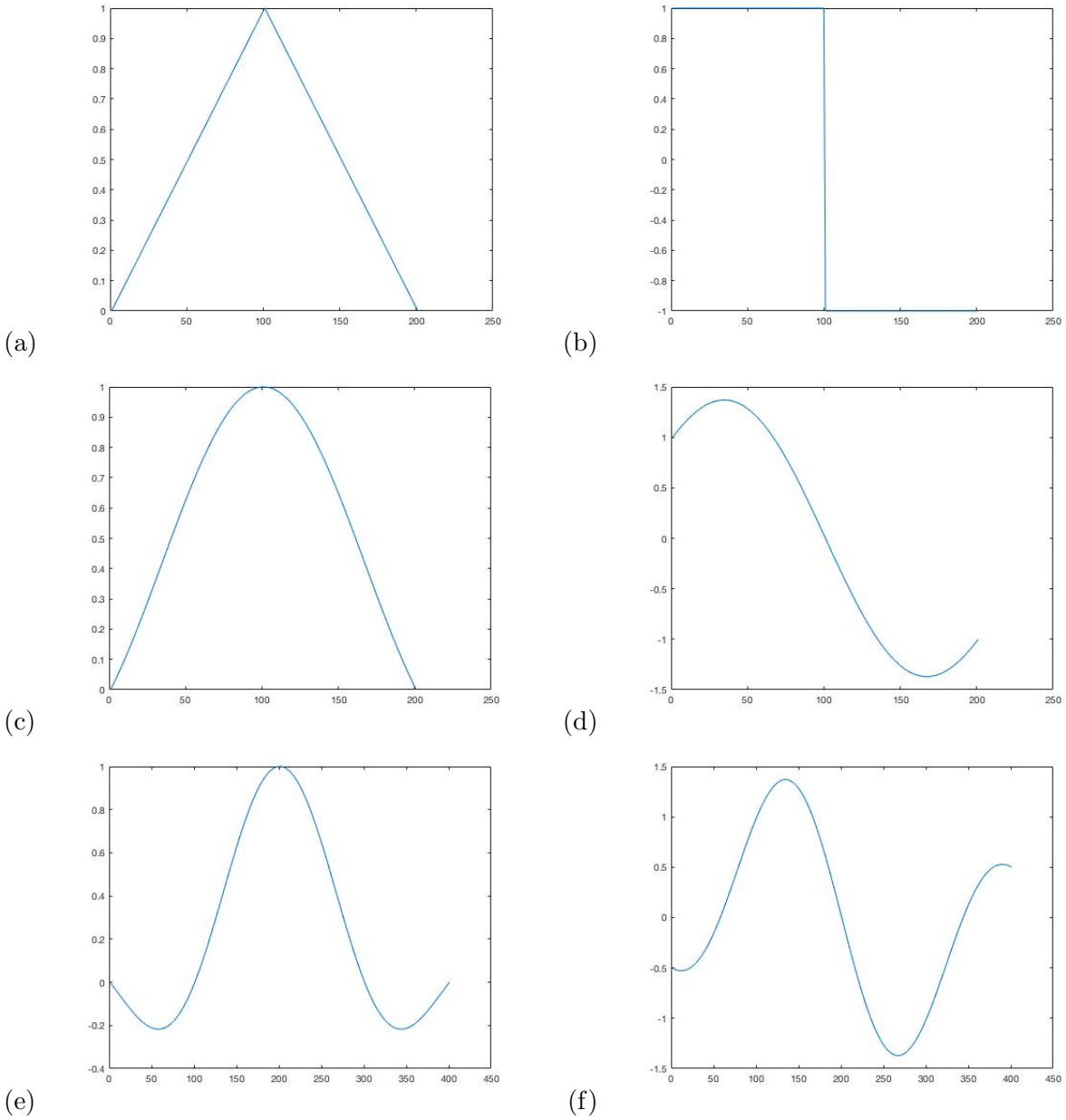

Figure 1: Trial functions and their derivatives for the different difference schemes covered in this paper. (a):Three-point spline function. (b): First derivative of a three-point spline function. (c):Three-point sinc function. (b): First derivative of a three-point sinc function. (e):Five-point sinc function. (b): First derivative of a five-point sinc function. The x-axis displays the number of points the function is interpolated with; on the y-axis the weight coefficient of the trial function.

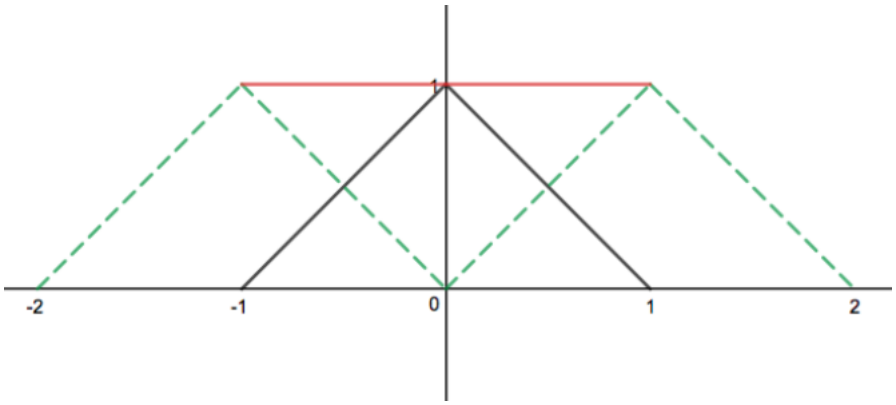

Figure 2: The overlap stencil for a three-point spline function in one dimension. The x-axis displays the gridpoints; the y-axis the weight coefficients. The dotted green spline functions depict the trial functions at $(z + \Delta z)$ and $(z - \Delta z)$ which are considered for the forward and backward difference. The sum of the overlap between the central trial function z_0 and $(z \pm \Delta z)$ is represented by the red line.

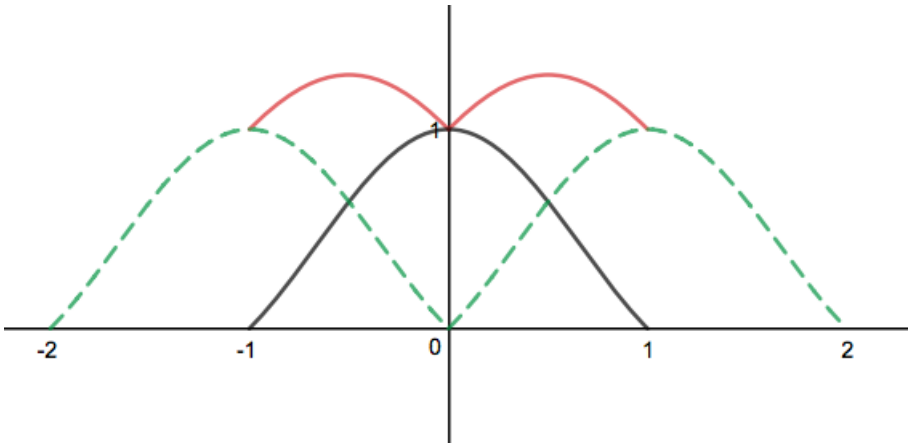

Figure 3: The overlap stencil for a three-point sinc function in one dimension.

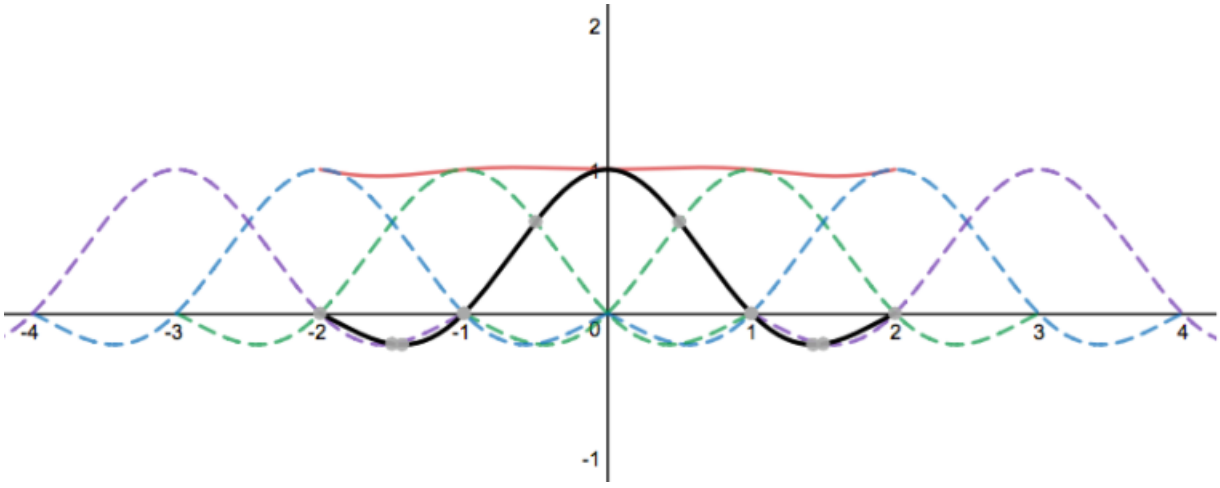

Figure 4: The overlap stencil for a five-point sinc function in one dimension. In black the sinc trial function at gridpoint z_0; $green for the trial functions at (z \pm \Delta z)$, blue for the trialfunctions at $(z \pm 2\Delta z)$ and purple for the trialfunctions at $(z \pm 3\Delta z)$. The red line is the joint contribution of the trial functions along the grid.

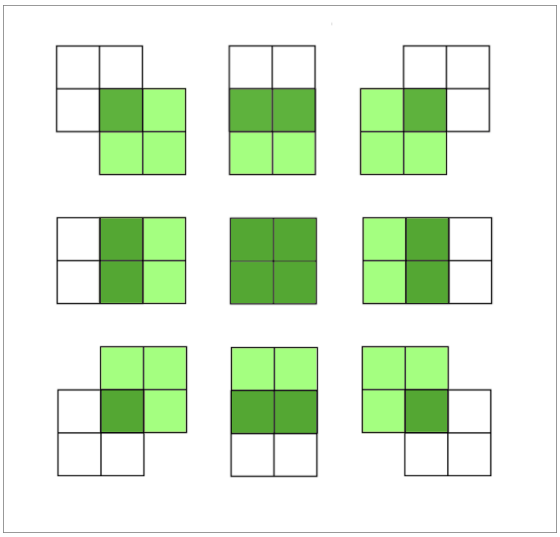

Figure 5: All the possible two-dimensional overlap scenarios for a three-point difference scheme between two arbitrary trial functions m (light green grid) and n (white grid). A dark green highlight annotates an area of overlap between the trial functions, which corresponds to its respective weight coefficient in the tables 7 to 16 , depending on the shape of the overlapping trial functions in question.

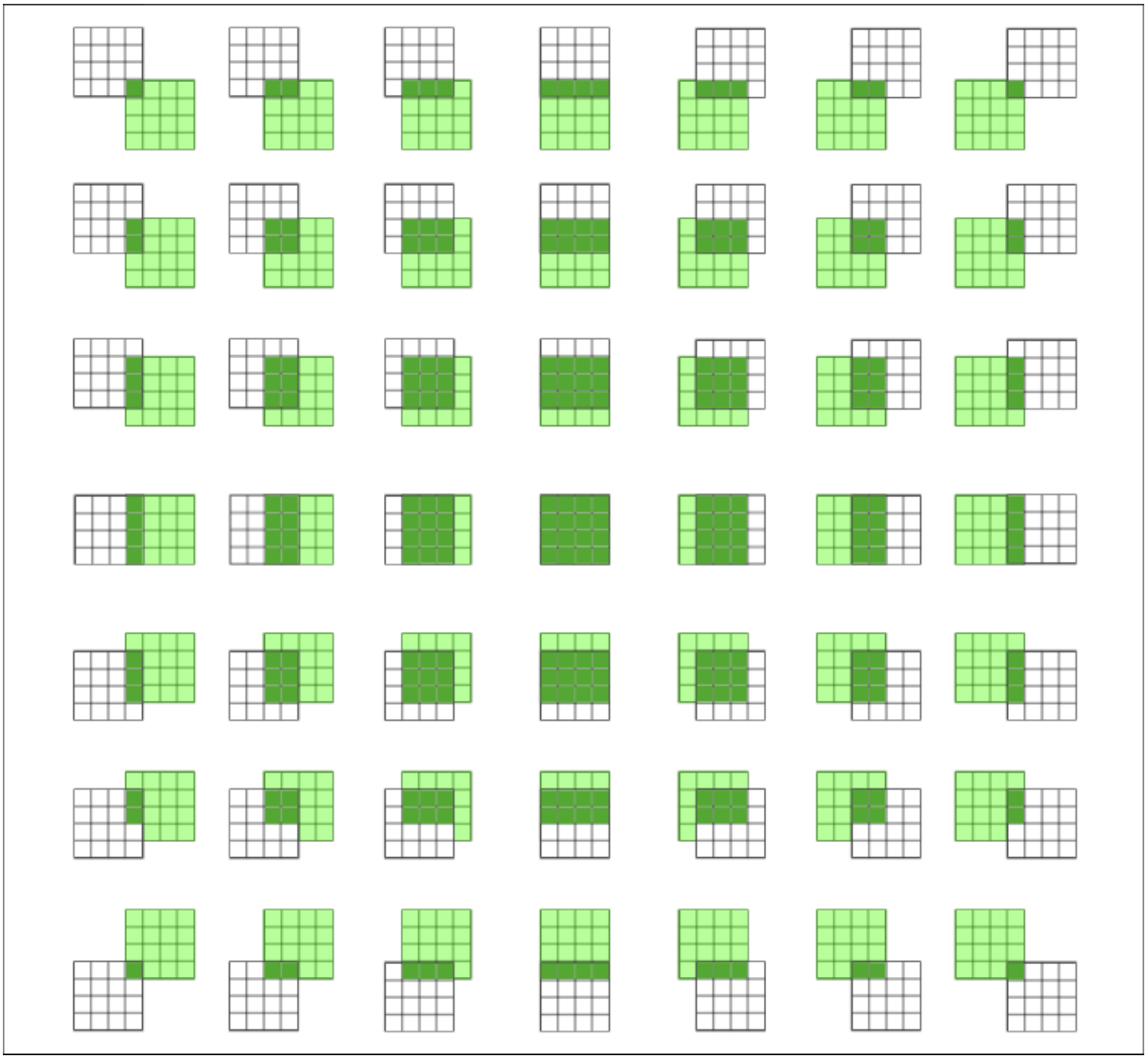

Figure 6: All the possible two-dimensional overlap scenarios for a five-point difference scheme between two arbitrary trial functions m (light green grid) and n (white grid). A dark green highlight annotates an area of overlap between the trial functions, which corresponds to its respective weight coefficient in the tables 17 to 21 , depending on the shape of the overlapping trial functions in question

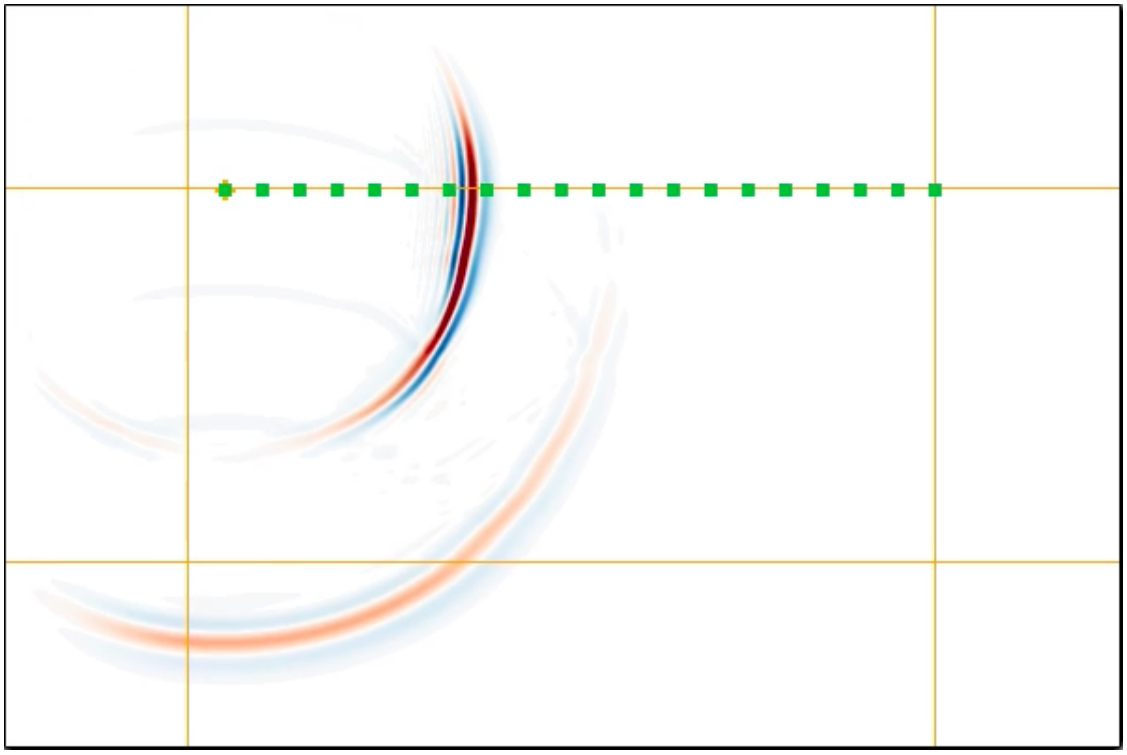

Figure 7: Two-dimensional waveform using the conventional operators for synthetic waveform generation.

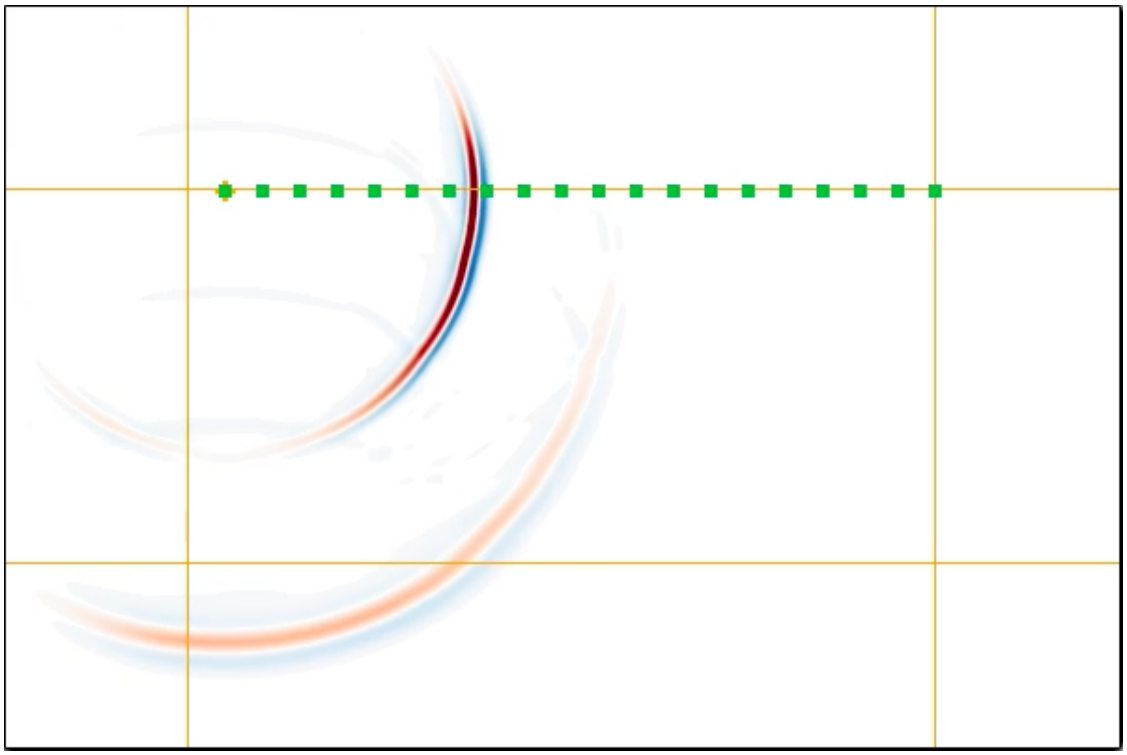

Figure 8: Two-dimensional waveform using the optimal operators for synthetic waveform generation.

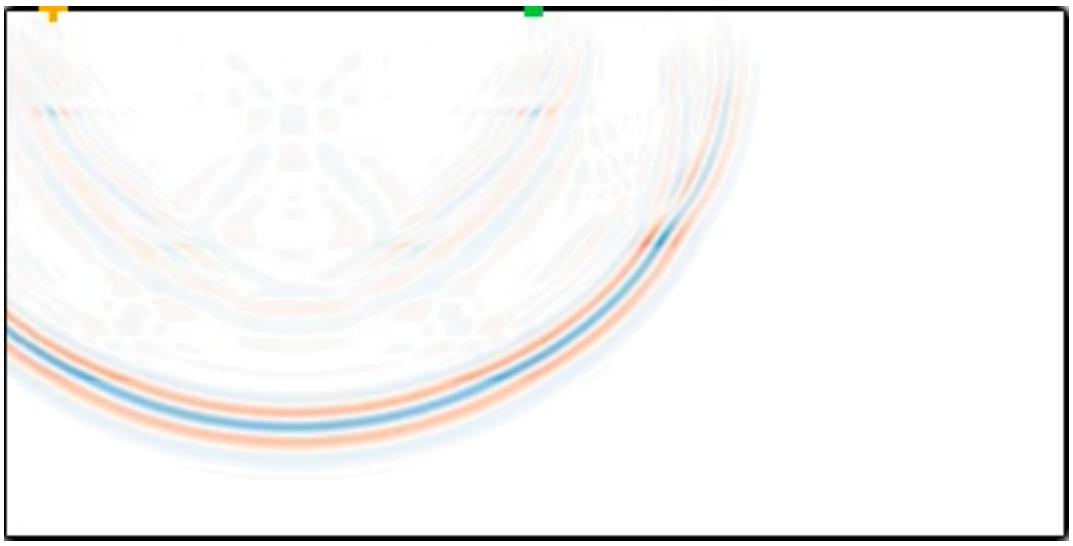

Figure 9: Two dimensional Frechet sensitivity kernels using conventional operators for the wave equation

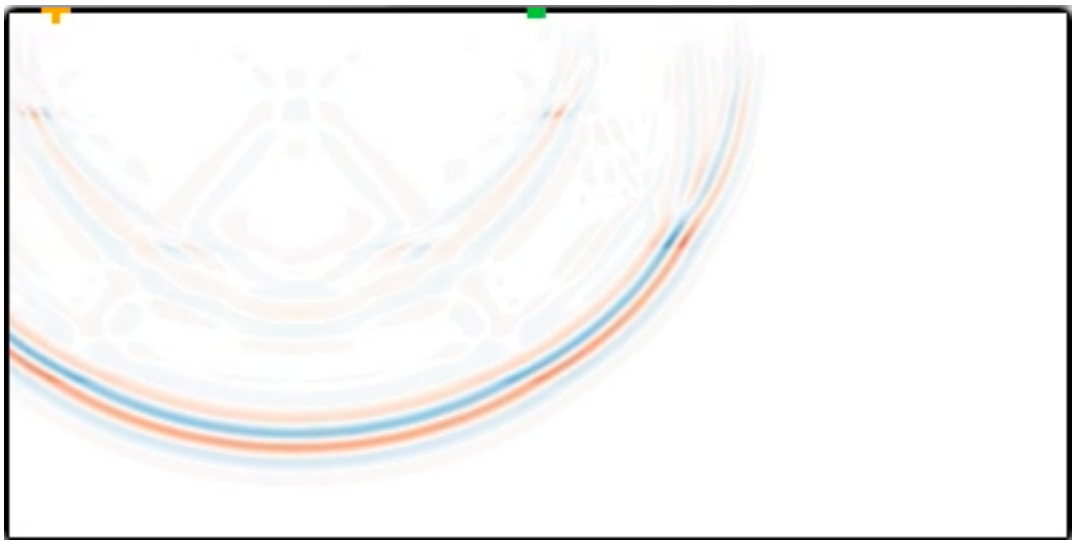

Figure 10: Two dimensional Frechet sensitivity kernels using optimal operators for the wave equation

Table 1: Trial function parameters for mass and stiffness matrices T and H1 for a three point spline function in a one-dimensional system containing five gridpoints, including free surface boundary conditions. Conforms to results of [Geller and Takeuchi, 1995]

1/3	1/6	0	0	0
1/6	2/3	1/6	0	0
0	1/6	2/3	1/6	0
0	0	1/6	2/3	1/6
0	0	0	1/6	1/3

Table 2: Trial function parameters for stiffness matrix H for a three point spline function in a one-dimensional system containing five gridpoints, including free surface boundary conditions. Conforms to results of [Geller and Takeuchi, 1995]

0.98	-1.0	0	0	0
-1.0	2.0	-1.0	0	0
0	-1.0	2.0	-1.0	0
0	0	-1.0	2.0	-1.0
0	0	0	-1.0	0.98

Table 3: Trial function parameters for mass and stiffness matrix T and H1 for a three point sinc function in a one-dimensional system containing five gridpoints, including free surface boundary conditions.

0.4514	0.2470	0	0	0
0.2470	0.9028	0.2470	0	0
0	0.2470	0.9028	0.2470	0
0	0	0.2470	0.9028	0.2470
0	0	0	0.2470	0.4514

Table 4: Trial function parameters for stiffness matrix H2 for a three point sinc function in a one-dimensional system containing five gridpoints, including free surface boundary conditions.

1.1515	-0.9591	0	0	0
-0.9591	2.3034	-0.9591	0	0
0	-0.9591	2.3034	-0.9591	0
0	0	-0.9591	2.3034	-0.9591
0	0	0	-0.9591	1.1515

Table 5: The one-dimensional weight coefficients for mass and stiffness matrix T and H1 at a central node m, calculated for five-point sinc functions according to the overlap stencil in Fig. 4

0.0229	-0.1578	0.0686	0.9499	0.0686	-0.1578	0.0229

Table 6: The one-dimensional weight coefficients for stiffness matrix component H2 at a central node m, calculated for the 1st order derivatives of five-point sinc trial functions according to the overlap stencil in Fig. 4

0.2153	-0.2408	-1.3132	2.7918	-1.3132	-0.2408	0.2153

Table 7: The two-dimensional weight coefficients for mass matrix T at a central node m, calculated for a three-point linear spline trial function according to the overlap stencil in Fig. 5

1/36	1/9	1/36
1/9	4/9	1/9
1/36	1/9	1/36

Table 8: The two-dimensional weight coefficients for stiffness matrix component H^{11} at a central node m, calculated for the joint contribution of three-point linear spline trial functions and their 1st order derivatives according to the overlap stencil in Fig. 5

- 1/6	1/3	- 1/6
- 2/3	4/3	- 2/3
- 1/6	1/3	- 1/6

Table 9: The two-dimensional weight coefficients for stiffness matrix component H^{33} at a central node m, calculated for the joint contribution of three-point linear spline trial functions and their 1st order derivatives according to the overlap stencil in Fig. 5

- 1/6	- 2/3	- 1/6
1/3	4/3	1/3
- 1/6	- 2/3	- 1/6

Table 10: The two-dimensional weight coefficients for stiffness matrix component H^{13} at a central node m, calculated for the joint contribution of three-point linear spline trial functions and their 1st order derivatives according to the overlap stencil in Fig. 5

- 1/4	0	1/4
0	0	0
1/4	0	- 1/4

Table 11: The two-dimensional weight coefficients for stiffness matrix component H^{31} at a central node m, calculated for the joint contribution of three-point linear spline trial functions and their 1st order derivatives according to the overlap stencil in Fig. 5

- 1/4	0	1/4
0	0	0
1/4	0	- 1/4

Table 12: The two-dimensional weight coefficients for overlapping mass matrix T at a central node m, calculated for the joint contribution of three-point sinc trial functions according to the overlap stencil in Fig. 5

0.061	0.223	0.061
0.223	0.8151	0.223
0.061	0.223	0.061

Table 13: The two-dimensional weight coefficients for overlapping stiffness matrix component H^{11} at a central node m, calculated for the joint contribution of three-point sinc trial functions and their 1st order derivatives according to the overlap stencil in Fig. 5

-0.236	0.569	-0.2369
-0.8659	2.0796	-0.8659
-0.2369	0.5689	-0.2369

Table 14: The two-dimensional weight coefficients for overlapping stiffness matrix component H^{33} at a central node m, calculated for the joint contribution of three-point sinc trial functions and their 1st order derivatives according to the overlap stencil in Fig. 5

-0.2369	-0.8659	-0.2369
0.5689	2.0796	0.5689
-0.2369	-0.8659	-0.2369

Table 15: The two-dimensional weight coefficients for overlapping stiffness matrix component H^{13} at a central node m, calculated for the joint contribution of three-point sinc trial functions and their 1st order derivatives according to the overlap stencil in Fig. 5

-0.4947	0	0.4877
0	0	0
0.4947	0	-0.4877

Table 16: The two-dimensional weight coefficients for overlapping stiffness matrix component H^{31} at a central node m, calculated for the joint contribution of three-point sinc trial functions and their 1st order derivatives according to the overlap stencil in Fig. 5

-0.4947	0	0.4947
0	0	0
0.4877	0	-0.4877

Table 17: The two-dimensional weight coefficients for overlapping mass matrix component T at a central node m, calculated for the joint contribution of five-point sinc trial functions according to the overlap stencil in Fig. 6

0.00052	-0.0036	0.0016	0.0217	0.0016	-0.0036	0.00052
-0.0036	0.0249	-0.0108	-0.1499	-0.0108	0.0249	-0.0036
0.0016	-0.0108	0.0047	0.0651	0.0047	-0.0108	0.0016
0.0217	-0.1499	0.0651	0.9024	0.0651	-0.1499	0.0217
0.0016	-0.0108	0.0047	0.0651	0.0047	-0.0108	0.0016
-0.0036	0.0249	-0.0108	-0.1499	-0.0108	0.0249	-0.0036
0.00052	-0.0036	0.0016	0.0217	0.0016	-0.0036	0.00052

Table 18: The two-dimensional weight coefficients for overlapping stiffness matrix component H^{11} at a central node m, calculated for the joint contribution of five-point sinc trial functions and their 1st order derivatives according to the overlap stencil in Fig. 6

0.0049	-0.0055	-0.0301	0.0638	-0.03	-0.0055	0.0049
-0.034	0.038	0.208	-0.4405	0.2072	0.038	-0.034
0.0148	-0.0165	-0.0904	0.1914	-0.09	-0.0165	0.0148
0.2045	-0.2288	-1.2522	2.6521	-1.2474	-0.2288	0.2045
0.0148	-0.0165	-0.0904	0.1914	-0.09	-0.0165	0.0148
-0.034	0.038	0.208	-0.4405	0.2072	0.038	-0.034
0.0049	-0.0055	-0.0301	0.0638	-0.03	-0.0055	0.0049

Table 19: The two-dimensional weight coefficients for overlapping stiffness matrix component H^{33} at a central node m, calculated for the joint contribution of five-point sinc trial functions and their 1st order derivatives according to the overlap stencil in Fig. 6

0.0049	-0.034	0.0148	0.2045	0.0148	-0.034	0.0049
-0.0055	0.038	-0.0165	-0.2288	-0.0165	0.038	-0.0055
-0.0301	0.208	-0.0904	1.2522	-0.0904	0.208	-0.0301
0.0638	-0.4405	0.1914	2.6521	0.1914	-0.4405	0.0638
-0.03	0.2072	-0.09	-1.2474	-0.09	0.2072	-0.03
-0.0055	0.038	-0.0165	-0.2288	-0.0165	0.038	-0.0055
0.0049	-0.034	0.0148	0.2045	0.0148	-0.034	0.0049

Table 20: The two-dimensional weight coefficients for overlapping stiffness matrix component H^{13} at a central node m, calculated for the joint contribution of five-point sinc trial functions and their 1st order derivatives according to the overlap stencil in Fig. 6

-0.00024	0.0049	-0.0154	0	0.0154	-0.0049	0.00024
0.0049	-0.1001	0.3173	0	-0.3173	0.1001	-0.0049
-0.0154	0.3123	-0.9899	0	0.9899	-0.3123	0.0154
0	0	0	0	0	0	0
0.0154	-0.3123	0.9899	0	-0.9899	0.3123	-0.0154
-0.0049	0.1001	-0.3173	0	0.3173	-0.1001	0.0049
0.00024	-0.0049	0.0154	0	-0.0154	0.0049	-0.00024

Table 21: The two-dimensional weight coefficients for overlapping stiffness matrix component H^{31} at a central node m, calculated for the joint contribution of five-point sinc trial functions and their 1st order derivatives according to the overlap stencil in Fig. 6

-0.00024	0.0049	-0.0154	0	0.0154	-0.0049	0.00024
0.0049	-0.1001	0.3123	0	-0.3123	0.1001	-0.0049
-0.0154	0.3173	-0.9899	0	0.9899	-0.3173	0.0154
0	0	0	0	0	0	0
0.0154	-0.3173	0.9899	0	-0.9899	0.3173	-0.0154
-0.0049	0.1001	-0.3123	0	0.3123	-0.1001	0.0049
0.00024	-0.0049	0.0154	0	-0.0154	0.0049	-0.00024